

# Robust Gravitational Wave Burst Detection and Source Localization in a Network of Interferometers Using Cross Wigner Spectra

Rocco P Croce<sup>1</sup>, Vincenzo Pierro<sup>1</sup>, Fabio Postiglione<sup>2</sup>,  
Maria Principe<sup>1</sup> and Innocenzo M Pinto<sup>1</sup>

<sup>1</sup>WavesGroup, University of Sannio at Benevento, Italy, INFN and LSC, <sup>2</sup> Dept. of Electronic and Computer Engineering, University of Salerno, Italy

E-mail: principe@unisannio.it

PACS number: 04.80.Nn, 07.05.Kf, 95.55.Sz

**Abstract.** We discuss a fast cross-Wigner transform based technique for detecting gravitational wave bursts, and estimating the direction of arrival, using a network of (three) non co-located interferometric detectors. The performances of the detector as a function of signal strength and source location, and the accuracy of the direction of arrival estimation are investigated by numerical simulations. The robustness of the method against instrumental glitches is illustrated.

## 1. Introduction

The next generation of interferometric detectors, of gravitational waves (henceforth GW) including AdLIGO [1], AdVirgo [2] and GEO-HF [3], hopefully to be followed soon by LCGT [4] and ACIGA [5], and eventually by ET [6], is expected to observe tens of events per year, opening the way to gravitational wave astronomy [7]. Identifying the direction of arrival (henceforth DOA) of the signals, and retrieving their shapes, will be a primary task in reconstructing the physics of the sources and their environments.

The possibility of retrieving the DOA from *independent* estimates of the signal arrival time at *each* detector was first suggested in [8], and further discussed in Saulson seminal book [9]. It was shown that three-interferometers are sufficient to retrieve the DOA up to a mirror-image ambiguity which can be solved in principle from knowledge of the detectors' directional responses. This method, often referred to as *triangulation* was further elaborated by Sylvestre [10], Cavalier et al. [11], and Merkovitz et al. [12]. In [11] a Gaussian distribution was assumed for the (independent) arrival time estimation errors, and a  $\chi^2$  minimization algorithm was accordingly proposed for retrieving the DOA, in the maximum likelihood spirit. In [12] it was shown that this method is affected by a systematic bias in the estimated DOA, a possible technique for removing the bias was discussed, and amplitude consistency tests for removing the mirror-image ambiguity were suggested. Fairhurst developed a similar analysis of the effect of arrival time estimation errors on the DOA estimation accuracy, for the special case of chirping signals, including waveform and calibration errors [13], [14].

DOA estimation algorithms are already implemented in the *coherent* LIGO-Virgo pipelines for GW burst (henceforth GWB) detection [15], [16]. DOA estimation in *coherent* network data analysis, was studied first by Krolak and Jaranowski [17], and

then by Pai et al. [18], as part of the waveform parameter estimation problem, with specific reference to chirping waveforms from coalescing binaries, in a Gaussian noise background. The conceptual foundations of coherent data analysis for unmodeled waveforms were laid out by Flanagan and Hughes [19], and further developed by Klimentko et al. [20]-[21]. Gürsel and Tinto [22] first suggested the possibility of retrieving the DOA for unmodeled signals using null-streams. This concept was analyzed in depth by Schutz and Wen [23], and further exploited by Chatterji et al. [24]. A Fisher-matrix based analysis of arrival time estimation error in coherent network detection of modeled as well as *unmodeled* signals was made in Wen et al. [25].

In this paper we capitalize on the time-shift and localization properties of the cross-Wigner-Ville (henceforth XWV) transform to introduce a new and conceptually simple GWB detection and DOA reconstruction algorithm, using a network of non co-located interferometric detectors.

The Wigner-Ville transform is a well known powerful tool for the analysis of non-stationary signals [26], whose potential in GW data analysis, has been highlighted by several Authors, under different perspectives [27]-[29]. Here we suggest its possible use as an effective tool for detecting GWBs, and estimating their DOA, which offers nice features in terms of performance, robustness against spurious instrumental/environmental transients (glitches).

Instead of using *independent* estimates of the arrival times at *each* detector, our DOA estimator uses data from (all) detector *pairs* to estimate the needed propagation delays. In addition, it also provides an effective detection statistic, combining the data from *all* detectors in the network, at a remarkably light computational cost.

DOA reconstruction from arrival-time delay estimation in a network of sensors is a well known problem in the technical Literature on Acoustics and Radar (see, e.g., [30] for a broad review). The standard method for time-delay estimation in Gaussian noise is (generalized) cross-correlation [31], which is known to perform reasonably well for relatively large signal to noise ratios [33]. Remarkably, the correlation-based estimator offers worse performances compared to the XWV in the present context, as shown in Sect. 5.2

This paper is organized as follows. In Sect. 2 we introduce the XWV transform, and recall its time-shift properties, which are illustrated for the simplest case of sine-Gaussian (henceforth SG) GWBs. In the same section we recall the relationship between arrival time delays and DOA. In Sect. 3, we illustrate the proposed XWV transform based DOA reconstruction algorithm. In Sect. 4 we discuss the effect of noise in the data, and the related DOA reconstruction uncertainties. In Sect. 5 we present the results of extensive numerical simulations, aimed at characterizing the performance of our XWV based algorithm both as a detector and as a DOA estimator. The simulations are based on SG-GWBs, but the case of more realistic waveforms (including Dimmelmeyer and binary merger waveforms) is also discussed. In Sect. 6 we include a short discussion of the robustness of the proposed algorithm against instrumental/environmental transients (glitches). Conclusions follow under Sect. 7.

## 2. Rationale. From Cross-Wigner-Ville Transforms to DOAs

In this section we recall a relevant property of the XWV transform, and illustrate it using ideal (sine-Gaussian) waveforms. We further recall the relationship between the

arrival time delays and the DOA, for a 3-detectors network, with special reference to the LIGO-Virgo Observatory.

### 2.1. Cross-Wigner-Ville Transforms

The XWV transform built from two (analytic, complex) signals  $\tilde{x}_{1,2}$  is given by [34], [35]:

$$W_{12}(t, f) = \int_{-\infty}^{\infty} d\theta \tilde{x}_1^* \left( t - \frac{\theta}{2} \right) \tilde{x}_2 \left( t + \frac{\theta}{2} \right) \exp(-2\pi i f \theta) \quad (1)$$

where  $*$  denotes complex conjugation. We recall that the so called *analytic signal* corresponding to a generic real-valued waveform  $x(t)$  is

$$\tilde{x}(t) = x(t) + i\mathcal{H}[x](t), \quad (2)$$

where  $\mathcal{H}[x](t)$  is the Hilbert transform [36]. For  $x_1(t) = x_2(t) = x(t)$ , eq. (1) reduces to the well known Wigner-Ville transform of  $x(t)$ .

### 2.2. Time-Shift Property of Cross-Wigner-Ville Transform

Let  $T_\theta$  the time-shift operator, such that

$$T_\theta[x] = x(t - \theta). \quad (3)$$

The following property of the XWV transform is easily proved:

$$W_{T_{\theta_1}[x_1], T_{\theta_2}[x_2]}(t, f) = \exp[-2\pi i f(\theta_2 - \theta_1)] W_{x_1, x_2} \left[ t - \frac{\theta_2 + \theta_1}{2}, f \right]. \quad (4)$$

Hence, if  $x_1$  and  $x_2$  are *the same* waveform  $x(t)$ , except for having different amplitudes, and different time-shift (delays), one accordingly has:

$$\left| W_{T_{\theta_1}[x_1], T_{\theta_2}[x_2]}(t, f) \right| = C \left| W_{x, x} \left[ t - \frac{\theta_2 + \theta_1}{2}, f \right] \right|. \quad (5)$$

where  $C$  is an irrelevant (positive) constant.

**2.2.1. Sine Gaussian GWBs** To illustrate the practical significance of eq. (5) in the context of GW detection of unmodeled transients using a network of interferometers, we shall refer here to SG waveforms, which have been widely used to model GWBs. More realistic transient waveforms will be considered in Section 5.3. Consider two SG waveforms, with common carrier frequency  $f_0$ , time spread  $T$ , and initial phases  $\phi_0$ , peaked at  $t_{1,2}$ , with amplitudes  $A_{1,2}$ , respectively, viz.:

$$x_i(t) = A_i \cos[2\pi f_0(t - t_i) + \phi_0] \exp[-(t - t_i)^2/T^2], \quad i = 1, 2 \quad (6)$$

Under the assumption  $f_0 T \gg 1$ , the analytic counterparts of (6) are asymptotically given by

$$\tilde{x}_i(t) \sim A_i \exp[2\pi i f_0(t - t_i) + i\phi_0] \exp[-(t - t_i)^2/T^2], \quad i = 1, 2 \quad (7)$$

The XWV spectrum, eq. (1) between  $\tilde{x}_1$  and  $\tilde{x}_2$  can be computed in closed form, yielding

$$W_{12}(t, f) = W_{21}(t, f) = (2\pi)^{1/2} A_1 A_2 T \exp[-2\pi^2 T^2 (f - f_0)^2].$$

$$\cdot \exp \left[ -\frac{2}{T^2} \left( t - \frac{t_1 + t_2}{2} \right)^2 \right] \exp [-2i\pi f(t_1 - t_2)]. \quad (8)$$

It is seen that  $|W_{12}(t, f)|$  is *peaked* at

$$t = \frac{t_1 + t_2}{2}, \quad f = f_0. \quad (9)$$

*2.2.2. Realistic Waveforms* The above *peak localization* property of the XWV holds true not only for SG waveforms, but essentially for *all* waveforms modeled by oscillatory transients with *unimodal* envelope, provided the product between the (instantaneous) carrier frequency and the envelope duration is a large number. Under this respect, the SG waveform is a kind of (worst) limiting case in view of its *minimal spread* property in the time frequency plane. Indeed, the localization property can be *more* marked for other transient waveforms, like, e.g., those numerically generated for supernovas or mergers, as discussed in Section 5.3.

### 2.3. XWV Spectra, Delays and DOAs

Let us confine for simplicity to the relevant case of the LIGO-Virgo network, which consists of the three large-baseline detectors located at Livingston LA (USA), Hanford WA (USA) and Cascina (Italy), henceforth denoted as L1, H1, and V, and labeled by the suffix  $i = 1, 2, 3$ , respectively. In the presence of a GWB, in view of eq. (9), the three XWV spectra computed from the data gathered by the LIGO-Virgo network interferometers will be (scaled) replicas of the Wigner-Ville transform of the observed GWB, exhibiting magnitude peaks at<sup>‡</sup>

$$t = T_{ij} = \frac{\tau_i + \tau_j}{2}, \quad f = f_{ij} = f_0, \quad \{i, j\} = \{1, 2\}, \{1, 3\}, \{2, 3\}, \quad (10)$$

where  $\tau_i$  is the GWB arrival time at detector- $i$ . Knowledge of the three  $T_{ij}$  from the corresponding XWV peaks allows to retrieve in principle two independent arrival-time delays, e.g.,

$$t_{13} = \tau_1 - \tau_3 = 2(T_{12} - T_{23}), \quad t_{23} = \tau_2 - \tau_3 = 2(T_{12} - T_{13}), \quad (11)$$

from which the DOA, and hence the source location on the celestial sphere can be uniquely inferred, as shown in the next subsection.

*2.3.1. DOA from Delays* The DOA is easily retrieved from the arrival-time delays using the reference system sketched in Figure 1, whose origin is the circumcenter  $O$  of the triangle whose vertexes are: (1) LIGO-Livingston (L1), (2) LIGO Hanford (H1), and (3) and Virgo (V), and whose  $x$ -axis goes, e.g., through L1. In this reference system the three detectors have spherical polar coordinates

$$(\vartheta_i = \pi/2, \varphi = \varphi_i), \quad i = 1, 2, 3 \quad (12)$$

and are located at:

$$\vec{r}_i = R(\hat{u}_x \cos \varphi_i + \hat{u}_y \sin \varphi_i), \quad i = 1, 2, 3 \quad (13)$$

<sup>‡</sup> We implicitly assume the interferometers' transfer functions as being frequency independent throughout the useful band of the sought signals.

where  $\varphi_1 = 0$  by construction, and  $R$  is the radius of the circumference through L1, H1 and V. Let the source polar coordinates and vector position be  $\vartheta = \vartheta_s, \varphi = \varphi_s$  and

$$\vec{r} = \rho(\sin \vartheta \cos \varphi \hat{u}_x + \sin \vartheta \sin \varphi \hat{u}_y + \cos \vartheta \hat{u}_z), \quad (14)$$

respectively, where  $\rho$  is the distance of the source from  $O$ . Under the obvious assumption where  $\rho \gg R$ , one has

$$|\vec{r} - \vec{r}_i| \sim \rho - R \sin \vartheta_s \cos(\varphi_s - \varphi_i), \quad i = 1, 2, 3. \quad (15)$$

whence the delays between the wavefront arrival times at the detectors are

$$t_{ij} = \tau_i - \tau_j = c^{-1} R \sin \vartheta_s [\cos(\varphi_s - \varphi_j) - \cos(\varphi_s - \varphi_i)], \quad (16)$$

$$\{i, j\} = \{1, 2\}, \{1, 3\}, \{2, 3\},$$

where  $c$  is the speed of light in vacuum. From the ratio  $\xi = t_{13}/t_{23}$  one may accordingly retrieve  $\varphi_s$  as follows,

$$\varphi_s = -\tan^{-1} \left[ \frac{(1 - \xi) \cos \varphi_3 + \xi \cos \varphi_2 - \cos \varphi_1}{(1 - \xi) \sin \varphi_3 + \xi \sin \varphi_2 - \sin \varphi_1} \right]. \quad (17)$$

Once  $\varphi_s$  has been computed, it can be used in (any of) eqs. (16) to retrieve  $\vartheta_s$ . Note that the delays (16) do *not* change upon letting  $\vartheta_s \rightarrow \pi - \vartheta_s$ , yielding the source mirror image w.r.t. to the detectors' plane. The above mirror-image ambiguity in a 3-detectors network is well known<sup>§</sup> [9].

#### 2.4. XWV Spectra of Noise

As a preparation for the next sections, it is important to characterize the key features of the XWV spectrum of independent, pure stationary Gaussian noise streams (the effect of instrumental transients, aka glitches, will be discussed in Sect. 6). In this case, the time-frequency levels in the XWV spectrum will be random, and their statistical distribution, in view of the assumed noise stationarity, will be the same for all (discrete) times.

The first two moments of the above distribution can be computed analytically with relative ease [37]. In particular, for all (discrete) frequencies the average value is zero, and the variance exhibits a piecewise linear dependence on frequency, as sketched in Figure 2. The maximum variance occurs at  $f = f_s/2$ , where  $f_s$  is the sampling frequency, and its value depends on the details of the XWV implementation (size, windowing), and the noise level in the data streams (see Appendix for details). It is thus expedient to *equalize* the XWV time-frequency levels, so as to obtain a uniform (flat) XWV spectrum for pure-noise data streams. To this end, we merely scale the XWV level in each time frequency pixel to the (computed) standard deviation of the XWV level in that pixel.

### 3. Estimating DOAs from Discrete XWV Spectra of Noisy Data

In practice, the XWV spectra will be computed in *discrete* form [34], yielding two-dimensional (complex) arrays, rather than continuous time-frequency functions over  $\mathbb{R}^2$ .

<sup>§</sup> The mirror-image ambiguity can be resolved, in principle, from knowledge of the detectors' pattern functions, featuring *different* responses in the  $\vartheta = \vartheta_s$  and  $\vartheta = \pi - \vartheta_s$  directions.

To minimize the effect of time-discretization error it is convenient to estimate the independent delays corresponding to the *largest* available baselines, i.e., in our case,  $t_{13}$  (L1-V) and  $t_{23}$  (H1-V).

Also, in the presence of noise eqs. (11) used in (16) will provide a mere *estimate* of the DOA, whose goodness will basically depend on the available signal to noise ratio, which affects the accuracy whereby the XWV peaks can be identified.

A simple algorithm for seeking peaks in the three LIGO-Virgo XWV spectra which are *consistent* with the constraints

$$\begin{cases} |t_{23}| = 2 |T_{12} - T_{13}| \leq c^{-1} |\vec{r}_{23}| \\ |t_{13}| = 2 |T_{23} - T_{12}| \leq c^{-1} |\vec{r}_{13}| \\ |t_{12}| = 2 |T_{23} - T_{13}| \leq c^{-1} |\vec{r}_{12}| \end{cases} \quad (18)$$

expressing the obvious requirements that the wavefront propagation delay between two detectors cannot exceed the limiting value corresponding to propagation along the line-of-sight direction between the detectors, can be now formulated. The algorithm uses the three (discrete, noisy) XWV spectra to construct a grid in the time delay plane  $(t_{13}, t_{23})$ , and assign different *levels*  $R$  to its nodes:

```

initialize all time-delay grid node levels to zero
for all time-frequency pairs  $(T_{12}, f_{12})$  in  $W_{12}$ 
  for all time-frequency pairs  $(T_{13}, f_{13})$  in  $W_{13}$  such that:
     $2|T_{12} - T_{13}| \leq c^{-1} |\vec{r}_{23}|$  and  $f_{13} = f_{12}$ 
      for all time-frequency pairs  $(T_{23}, f_{23})$  in  $W_{23}$  such that:
         $2|T_{12} - T_{23}| \leq c^{-1} |\vec{r}_{13}|$  and  $f_{23} = f_{12}$ 
          accumulate level  $R = R + |W_{12}(T_{12}, f_{12})W_{13}(T_{13}, f_{13})W_{23}(T_{23}, f_{23})|$ 
          at grid node  $\{t_{13} = 2(T_{12} - T_{23}), t_{23} = 2(T_{12} - T_{13})\}$ 
        end for
      end for
    end for
  end for
end for.
```

A *candidate* direction of arrival is obtained by taking the highest-level grid-node in the  $(t_{13}, t_{23})$  plane subset defined by the further constraint<sup>||</sup>.

$$|t_{12}| = |t_{13} - t_{23}| \leq c^{-1} |\vec{r}_{12}| \quad (19)$$

The highest level in the grid can be used both as an *estimator* of the DOA, and as a *detection statistic*, whose performances will be discussed in Sect. 5.1.

Note that the proposed algorithm is *coherent*, in the sense that it produces a *single* detection statistic by combining the data from *all* detectors in the network. It also inherits the typical features of *coincident* tests: the outermost loop enforces frequency-consistency, while the two inner loops enforce time-delay *admissibility*.

Note also that the XWV spectra will display sensible peaks only if the waveform gathered by the different detectors are *consistent in shape*. This suggests that the algorithm will be robust against (independent) instrumental disturbances, as further illustrated in Sect. 6.

<sup>||</sup> As shown in Sect. 4, the bound in (19) can be made slightly tighter.

### 3.1. LIGO-Virgo Network Directional Response under XWV Based Algorithm

In the absence of noise, the above algorithm will produce a peak in the time-delay grid whenever a GWB is observed by the LIGO Virgo network. The peak will be located at a node whose time-delay coordinates correspond to the DOA  $(\vartheta_s, \varphi_s)$ . This peak will be well localized provided the duration of the transient signal is substantially shorter than the minimum graviton flight-time between detectors.

In view of the bilinear nature of the XWV, it can be argued that the peak height will be proportional to the squared product of the three detectors' pattern functions along that direction. This quantity, normalized to its maximum, and denoted henceforth as  $\bar{\Phi}(\vartheta, \varphi)$  describes the directional response of the proposed GWB detector/DOA estimator, and is plotted in Figure 3 for the LIGO-Virgo network, for circularly polarized GWs. We checked numerically that the expected (normalized) levels of the time-delay grid peaks, reproduce those computed from the function  $\bar{\Phi}$  for each DOA in a  $\vartheta, \varphi$  grid of  $50 \times 100$  points (using  $10^3$  noise realization for each DOA).

The quantity:

$$\frac{\Omega[\bar{\Phi}_{min}]}{4\pi} = \frac{1}{4\pi} \int_{\bar{\Phi}(\vartheta, \varphi) > \bar{\Phi}_{min}} \sin \vartheta d\vartheta d\varphi \quad (20)$$

expresses the *fraction* of the (unit) celestial sphere where the (normalized) directional response of the proposed detector/estimator exceeds the threshold value  $\bar{\Phi}_{min}$ , and is displayed in Figure 4.

It is seen, e.g., that roughly 50% of the celestial sphere is covered with  $\bar{\Phi}_{min} \geq .2$  by the LIGO-Virgo network, using the proposed algorithm.

## 4. DOA Reconstruction Uncertainties

Uncertainties in the DOA reconstruction stem from a twofold origin: the discreteness of the time-delay grid, due to the discrete implementation of the XWV spectra (finite time resolution), and the additive noise in the data (see discussion in Sect. 5.2).

In order to translate the effect of systematic and statistical errors in the estimated delays into uncertainty ranges in the estimated DOAs, it is expedient to introduce the projection which maps the DOA polar angles  $(\vartheta_s, \varphi_s)$  into a point  $(x_s, y_s)$  of the disc (with center  $O$  and radius  $R$ ) going through the detector, viz. ¶:

$$x_s = R \sin \vartheta_s \cos \varphi_s, \quad y_s = R \sin \vartheta_s \sin \varphi_s. \quad (21)$$

The formula which relates the  $(x_s, y_s)$  projection to the arrival-time delays is obtained from eq. (16),

$$\begin{cases} x_s = c \frac{(t_{13} - t_{23}) \sin \varphi_3 - t_{13} \sin \varphi_2}{-\sin(\varphi_2 - \varphi_3) + \sin \varphi_2 - \sin \varphi_3} \\ y_s = c \frac{t_{13} \cos \varphi_2 - (t_{13} - t_{23}) \cos \varphi_3 - t_{23}}{-\sin(\varphi_2 - \varphi_3) + \sin \varphi_2 - \sin \varphi_3} \end{cases} \quad (22)$$

Equation (22) is a *linear* transformation, relating not only the coordinates  $(x_s, y_s)$  to the delays  $(t_{13}, t_{23})$ , but also the *uncertainties*  $\delta x_s, \delta y_s$  to the delay errors  $\delta t_{13}$  and  $\delta t_{23}$ . Thus, under the simplest assumption where these latter are independent and identically distributed, the uncertainty region in the  $(t_{13}, t_{23})$  plane is a circle, and

¶ We recall that the  $x$ -axis goes through detector-1 (LIGO-Livingston).

the corresponding uncertainty region in the  $(x_s, y_s)$  plane is an *ellipse*. Notably, the *shape* of this latter is translation-invariant across the circle  $x_s^2 + y_s^2 \leq R^2$ , i.e., DOA independent.

The ratio between the uncertainty areas in the  $(x_s, y_s)$  and  $(t_{13}, t_{23})$  planes is given by the Jacobian of the transformation (22), viz.:

$$J = c^2 \frac{\sin(\varphi_3 - \varphi_2)}{\sin \varphi_3 - \sin \varphi_2 + \sin(\varphi_2 - \varphi_3)} \quad (23)$$

which is also DOA-independent.

By back-projecting the uncertainty ellipse onto the sphere of radius  $R$  centered at  $O$ , we obtain a DOA-dependent uncertainty region. This is illustrated in Figure 5, for a few representative cases. The ratio between the area of the uncertainty region on the celestial sphere, and the area of the uncertainty ellipse in the  $(x_s, y_s)$  plane is displayed in Figures 6a and 6b as a function of  $\varphi_s$ , for various values of  $\vartheta_s$ . For  $\vartheta_s \sim 0$ , this ratio is close to unity, whatever  $\varphi_s$ . On the other hand as  $\vartheta_s \rightarrow \pi/2$ , the ratio blows up, and its dependency on  $\varphi_s$  becomes more and more evident. Such a behaviour had been already noted in, e.g., [11], [13].

## 5. Numerical Experiments

In order to check the performance of the proposed algorithm, we run a series of Monte Carlo simulations. The simulations use time-discretized GWBs and glitches injected into white (independent) random Gaussian sequences, to represent the three interferometer data. In the case of GWBs, the delays are chosen according to the assumed source location.

Our XWV engine uses data chunks 2048 time-samples wide to produce a  $1024 \times 1024$  time-frequency nodes XWV transform, using Pei-Yang fast algorithm [38]. The sampling frequency is  $4 \text{ KHz}$ . The data are accordingly decomposed into half-overlapping chunks 2048 time-samples wide (we use a plain rectangular windowing function), in order to use a fixed number of time samples to compute each time-frequency samples. The resulting discrete XWV spectrum spans the time range between samples #513 and #1536, and the frequency range between 0 and  $1000 \text{ Hz}^+$ . As already mentioned, the XWV values are equalized so that in the absence of signals their first and second moment are 0 and 1, respectively.

Now, even in the absence of a signal, the levels produced by our algorithm in the time-delay plane  $(t_{13}, t_{23})$  grid-nodes will be *non-uniform*, due to the *different* number of (noisy) time-frequency XWV values mapped into each node. The average and standard deviation in the  $(t_{13}, t_{23})$  plane for pure-noise (stationary, Gaussian) data are shown in Figure 7. We accordingly *equalize* the levels, by subtracting the above average, and dividing the result by the above standard deviation, so that in the absence of signals, the grid-node levels in the time-delay plane will have zero average and unit variance. For each injected waveform, we generated  $10^4$  different noise realizations, to test the statistical properties of the proposed algorithm, both as a detector and as a DOA estimator. The waveforms were parameterized by their *intrinsic* signal to noise ratio (SNR), defined by

$$\delta_h = \frac{h_{rss}}{N} = \frac{\left\{ \int [h_+^2(t) + h_\times^2(t)] dt \right\}^{1/2}}{N}, \quad (24)$$

<sup>+</sup> Note that when using analytic signals for computing discrete versions of the XWVT, the minimum sampling rate must be *twice* the Shannon rate [34]



$N$  being the (two-sided) power spectral density of the stationary white(ned) Gaussian noise component, assumed for simplicity the same in all detectors (the effect of glitches will be discussed in Sect. 6).

The results of our simulations are summarized below.

### 5.1. Detection Performance

The performance of our algorithm as a detector are illustrated in Figures 8 and 9. The detection statistic is the level of the highest peak in the time-delay grid. Figure 8a and 8b display the false alarm (continuous line) and false dismissal probabilities (the dashed lines, corresponding to different values of the intrinsic SNR ( $\delta_h$ ) as functions of the detection threshold  $\gamma$ , for DOAs corresponding to the maximum ( $\vartheta = 0.705rad$ ,  $\varphi = 5.073rad$ ) and the minimum ( $\vartheta = 0.800rad$ ,  $\varphi = 1.100rad$ ) of the network pattern function in Fig. 3. Figures 9a and 9b show the receiver operating characteristics, i.e., the detection probability vs the false alarm probability, for fixed values of the intrinsic signal to noise ratio,  $\delta_h$ , for a DOA corresponding to the maximum of the network pattern function in Fig. 3.

### 5.2. DOA Estimation Performance

As already mentioned, the finite time resolution implies that the estimated delays are affected by a *systematic* uncertainty which can be twice the XWV time-step  $\delta t$ . The noise in the data entails that estimated delays *spread* around the *actual* delays in a signal-to-noise dependent way. This is illustrated in Figures 10 and 11. The estimate is always unbiased, whenever the signals are shorter than the minimum graviton flight time between the detectors. Figure 10 displays the standard deviation of the estimated delays (average between the two) as a function of the intrinsic SNR, for DOAs corresponding to the maximum ( $\vartheta = 0.705rad$ ,  $\varphi = 5.073rad$ ) and the minimum ( $\vartheta = 0.800rad$ ,  $\varphi = 1.100rad$ ) of the network pattern function in Fig. 3. In a log-log scale, both curves show the same slope, corresponding to an exponent  $\approx -1.4$ . Figure 11a displays the empirical distribution of the estimated delays for  $10^4$  different noise realizations, for a DOA corresponding to the maximum of the network pattern function in Fig. 3, for two different values of the intrinsic signal to noise ratio. It is interesting to compare Fig. 11a to Fig. 11b, where a standard correlation-based time-delay estimator [39] has been used to retrieve the two propagation delays. Our XWV-based estimator is seen to offer distinctly better performances.

### 5.3. Realistic Waveforms

As anticipated in Section 2, the XWV transform peak localization property holds not only for SG waveforms, but for general transient waveforms. This is further illustrated in Figures 12 to 15.

Figure 12 (top) shows two copies of a typical supernova GWBs, belonging to the family computed by Dimmellaier and co-workers [40], with a time shift of 82 time samples (corresponding to 20.5 ms, at our sampling frequency), together with their XWV transform. The XWV is identical to the Wigner transform of the GWB waveform, except for the time-shift given by eq. (5). Accordingly, the XWV peak in Fig. 12 (bottom) is localized at the midpoint between the peak times of the two waveforms in Fig. 12 (top). Figure 13 (left) shows the time-delay grid histogram when this waveform is emitted by a source located in the direction of maximum network sensitivity in Fig.

3, for  $\delta_h = 100$ . It can be seen that, not unexpectedly, the localization properties in the delay plane are even better than for Gaussian waveforms, in view of the larger time-bandwidth figure of the Dimmelmaier waveform.

Figures 14 and 15 are similar to Figs. 12 and 13, except that the waveform here is that of a typical binary merger [41].

## 6. Glitch Rejection

By construction the proposed detection/localization algorithm should be robust against spurious transients of environmental/instrumental origin (glitches).

We may expect that glitch induced false detection may occur only in the (unlikely) case where *each* detector shows a glitch in the analysis window, such that the mutual delays are consistent with an acceptable DOA, *and* the (independent) glitch waveforms are *consistent* in shape.

In order to illustrate these features, we consider first the no-GWB case where a glitch occurs in the data of *each* of the three interferometers, the three glitches being *different*, but with delays consistent with an *admissible* DOA.

To this end, we used a set of  $N = 7$  visually different waveforms, shown in Figure 16 (top), from the catalogue of "typical" LIGO glitches compiled by P. Saulson [42]. All glitches in the set were scaled to unit norm, and time-shifted so as to bring their envelope peaks to coincidence. The (normalized) pairwise correlation coefficient of the selected glitches, which provides some quantitative measure of their (dis)-similarity, does not exceed 0.62, with mean and median values of 0.195 and 0.105, respectively. The correlation coefficient histogram is shown in Figure 16 (bottom left).

From the above glitch set, we formed (all) 35 triplets of *different* waveforms, and computed the related X-Wigner transforms and the peak-levels in the time-delay grid produced by our algorithm. For each of glitch-triplet  $(g_1, g_2, g_3)$  we also computed the geometric mean of the time-delay grid peak-levels for the three cases where the data from *all* interferometers contain the *same* waveform  $* g_i$ ,  $i = 1, 2, 3$ . This quantity was used to re-scale the time-delay grid peak-level for that glitch-triplet.

The histogram of the rescaled time-delay grid peak-levels for the 35 different glitch triplets considered is shown in Figure 16 (bottom right). The largest (scaled) peak level was 0.51, with a median value of 0.12 and a mean of 0.17.

These, admittedly limited, results illustrate the waveform consistency test capabilities of the proposed algorithm.

We next consider the case where GWBs *and* glitches co-exist in the data. In these further simulations we used SG glitches and GWBs, with glitch parameters (center frequency, peak position and carrier frequency) generated randomly and independently in each detector. The pertinent results are illustrated in Figures 17 to 20. These figures show the noisy waveforms (left column), the density maps of the XWV transforms (mid column), and the (normalized) level map in the  $(t_{12}, t_{13})$  time-delay grid. In Fig. 17 we consider the simplest case where the GWB data in a single detector (H1 in this case) are corrupted by a single glitch in the analysis window. The GWB signal to noise ratios are 22.16 (L1), 23.13 (H1) and 31.85 (V), for a (circularly polarized)

\* These correspond to a source *equidistant* from all detectors radiating the waveform  $g_i$ , with all detectors exhibiting the *same* response in the source direction. The last assumption is unrealistic, but is irrelevant for the present purpose).

source with  $\delta_h = 50$  at  $\vartheta = 2.58rad$  and  $\varphi = 2.71rad$ . The glitch signal to noise ratio in H1 is 22.59. The glitch shows up clearly in the H1 data, and produces evident artifacts in the H1-V and H1-L1 XWV spectra. Nonetheless, its effect on the time-delay level map is almost negligible.

In Fig. 18 we consider the (unlikely) case where the data in *each* detector are corrupted by (single) glitches in the analysis window, with SNR values of 11.5 (L1), 12.00 (H1) and 16.53 (V). None of the glitches has a significant overlap with the GWBs; nonetheless, they produce artifacts in all XWV transforms. Also in this case the effect of these artifacts on the detection/localization properties is negligible, as seen from the time-delay level map.

Not unexpectedly, the localization performance deteriorates significantly in the rather extreme situation where glitches *overlap* the GWBs in the data. When this happens in such a way that *true* peaks in the XWV transforms are no longer *resolvable* from spurious ones, the time delay level map topography is substantially blurred in the neighbourhood of the *true* delays, resulting into more or less severe localization errors. This is illustrated in Figs. 19 and 20.

In Fig. 19 we have a (single) GWB-overlapping glitch in H1 with SNR=16.28. In Fig. 20 each detector is affected by a GWB-overlapping glitch. The glitch SNR values in Figs. 19 and 20 are the same as those in Figs. 17 and 18. A sensible distortion in the XWV transforms is observed, entailing a sensible error in the estimated delays.

## 7. Conclusions

We presented a simple, computationally light and fast algorithm for detecting short unmodeled GWB in a network of three interferometric GW detectors, and estimating the related DOA, based on XWV spectra. The algorithm is reasonably performant, and nicely robust against spurious transients (glitches) of instrumental origin corrupting the (otherwise Gaussian) detectors noise floor.

It does not provide waveform reconstruction; this latter, however can be accomplished in principle off-line, once the DOA has been estimated.

Generalization to larger networks, and other potentially interesting waveforms (e.g., chirps) is relatively straightforward. Such extensions will be explored in a forthcoming paper.

Based on the above preliminary results, we suggest that the proposed algorithm may be used as a quick-and-(not-so)-dirty on-line data sieving tool.

A quantitative comparison with existing GWB detection/DOA estimation algorithms in terms of efficiency and computational burden will be the subject of future investigation.

## Acknowledgements

We thank the anonymous Referees for several useful suggestions and remarks.

## References

- [1] <http://www.advancedligo.mit.edu>
- [2] <https://www.casina.virgo.infn.it/advirgo>
- [3] B. Willke et al., "The GEO-HF Project," *Class. Quantum Grav.* **23** (2006) S207.
- [4] <http://gw.icrr.u-tokyo.ac.jp/lcgt>
- [5] <http://www.anu.edu.au/physics/ACIGA>
- [6] <http://www.et-gw.eu>

- [7] N Anderson and K D Kokkotas, "Gravitational Wave Astronomy: The High Frequency Window," *Lecture Notes in Physics*, **653** (2005) 255.
- [8] J.L. Boulanger et al., "Towards the Birth of Gravitational Wave Astronomy. II. Directivity and Number of Events in Coincidences Expected from Gravitational Wave Detection by Interferometry," *Astron. Astrophys.* **217** (1989) 381.
- [9] P Saulson, "*Fundamentals of Interferometric Gravitational Wave Detectors*," World Scientific, 1994.
- [10] J. Sylvestre, "Prospects for the Detection of Electromagnetic Counterparts to Gravitational Wave Events," *The Astrophys. J.*, **591** (2003) 1152.
- [11] F. Cavalier et al., "Reconstruction of Source Location in a Network of Gravitational Wave Interferometric Detectors," *Phys. Rev.* **D74** (2006) 082004.
- [12] J. Markowitz et al., "Gravitational Wave Burst Source Direction Estimation Using Time and Amplitude Information," *Phys. Rev.* **D 78** (2008) 122003.
- [13] S. Fairhurst, "Triangulation of Gravitational Wave Sources with a Network of Detectors," *New J. Phys.* **11** (2009) 123006.
- [14] S Fairhurst, "Source Localization with an Advanced Gravitational Wave Detector Network," *Class. Quantum Grav.* **28** (2011) 105021.
- [15] P J Sutton et al., "X-Pipeline: an Analysis Package for Autonomous Gravitational-Wave Burst Searches," *New J. Phys.* **12** (2010) 053034.
- [16] S. Klimenko et al., "Localization of Gravitational Wave Sources with Networks of Advanced Detectors," *Phys. Rev.* **D83** (2011) 102001.
- [17] P Jaranowski and A Krolak, "Optimal Solution of Inverse Problem for Gravitational Wave Signal of a Coalescing Compact Binary," *Phys. Rev.* **B49** (1994) 1723..
- [18] A Pai, S Dhurandhar and S Bose, Data Analysis Strategy for Detecting Gravitational-Wave Signals from Inspiring Compact Binaries with a Network of Laser-Interferometric Detectors, *Phys. Rev.* **D64** (2001) 042004.
- [19] É.E. Flanagan and S.A. Hughes, "Measuring Gravitational Waves from Binary Black Hole Coalescences: II. The Waves' Information and its Extraction, with and without Merger Templates," *Phys. Rev.* **D57** (1998) 4566.
- [20] S. Klimenko et al., "Constraint Likelihood Analysis for a Network of Gravitational Wave Detectors," *Phys. Rev.* **D72** (2005) 122002.
- [21] M. Rakhmanov, Rank Deficiency and Tikhonov Regularization in the Inverse Problem for Gravitational Wave Bursts," *Class. Quantum. Grav.*, **23** (2006) S673
- [22] Y Gursel and M Tinto, "Near Optimal Solution to the Inverse Problem for Gravitational-Wave Bursts," *Phys. Rev.* **D40** (1989) 3884.
- [23] L Wen and B F Schutz, "Coherent Network Detection of Gravitational Waves: the Redundancy Veto," *Class. Quantum Grav.* **22** (2005) S1321.
- [24] S. Chatterji et al., "Coherent Network Analysis Technique for Discriminating GW Bursts from Instrumental Noise," *Phys. Rev.* **D74** (2006) 082005.
- [25] L Wen, X Fan and Y Chen, "Geometrical Expression of the Angular Resolution of a Network of Gravitational-Wave Detectors and Improved Location Methods" *J. Phys. Conf. Ser.* **122** (2008) 012038.
- [26] T. A. C. M. Claasen and W. F. G. Mecklenbrauker, The Wigner DistributionA Tool for Time-Frequency Signal Analysis, Part I: Continuous- Time Signals, *Philips J. Res.*, **35** (1980) 217.
- [27] M. Feo et al., "Efficient GW Chirp Detection and Estimation via Time-Frequency Analysis and Edge Detection," in *VII Marcel Grossman Meeting on General Relativity*, R.T. Jantzen et al., Eds., World Scientific, Singapore (1996) p. 1086.
- [28] W.G. Anderson and R. Balasubramanian. "Time-Frequency Detection of Gravitational Waves," *Phys. Rev.* **D60** (1999) 102001.
- [29] E. Chassande-Mottin and P. Flandrin, "On the Time-Frequency Detection of Chirps," *Appl. Comp. Harm. Anal.*, **6** (1999) 252.
- [30] B. Berdugo et al., "On Direction Finding of an Emitting Source from Time Delays," *J. Acoust. Soc. Am.*, **105** (1999) 3355.
- [31] C.H. Knapp and G.C. Carter, "The Generalized Correlation Method for Estimation of Time Delay," *IEEE Trans. Acoustic Speech and Signal Proc.*, **24** (1976) 320.
- [32] J. Chen, J. Benesty, and Y. Huang, Robust Time Delay Estimation Exploiting Redundancy Among Multiple Microphones, *IEEE Trans. Speech Audio Process.*, **11** (2003) 549.
- [33] A. Fertner and A. Sjolund, "Comparison of Various Time Delay Estimation Methods by Computer Simulation," *IEEE Trans. Acoustic Speech and Signal Proc.*, **24** (1986) 1329.
- [34] T. A. C. M. Claasen and W. F. G. Mecklenbrauker, "The Wigner DistributionA Tool for Time-Frequency Signal Analysis, Part II: Discrete- Time Signals, *Philips J. Res.*, **35** (1980) 276.
- [35] T. A. C. M. Claasen and W. F. G. Mecklenbrauker, The Wigner DistributionA Tool for Time-Frequency Signal Analysis, Part III: Relations with Other Time-Frequency Signal Transformations, *Philips J. Res.*, **35** (1980) 372.
- [36] A.V. Oppenheim and R.W. Schaffer, "*Discrete-Time Signal Processing*," Prentice Hall, 2009.
- [37] L. Stanković and S. Stanković, "On the Wigner Distribution of Discrete-Time Noisy Signals

- with Applications to the Study of Quantization Effects," IEEE Trans. on Signal. Proc., **42** (1994) 1863.
- [38] S.C. Pei, I.I. Yang, "Computing Pseudo-Wigner Distribution by the Fast Hartley Transform," IEEE Trans. **SP-40** (1992) 2346.
- [39] S. Lawrence Marple, "Estimating Group Delay and Phase Delay via Discrete Time Analytic Cross Correlation," IEEE Trans. Signal Proc. **47** (1999) 2604.
- [40] H. Dimmelmeier, C.D. Ott, A. Marek and H.T. Janka, "Gravitational Wave Burst Signal from Core Collapse of Rotating Stars," Phys. Rev. **D78** (2008) 064056.
- [41] J.G. Baker et al., "Comparisons of Binary Black hole Merger Waveforms", Class. Quant. Grav. **24** (2007) S25.
- [42] P. Saulson, "Listening to Glitches," LIGO Document G070548 (2007).

**Appendix - XWV Moments.**

Let

$$W_{f,g}(n, m) = \sum_{k=-L}^L f(n+k)g^*(n-k) \exp[-4iN^{-1}\pi mk]. \quad (25)$$

the discrete version of the XWV spectrum, where  $n$  and  $k$  are the discrete time and frequency index. Note that, formally,

$$W_{f,g}(n_0, m) = DFT_x(2m) \quad (26)$$

where  $x = f(n_0 + k)g^*(n_0 - k)$ . This shows that while the time index  $n$  spans the range  $(-L, L) \cap \mathbb{N}$ , the frequency index  $m$  spans the range  $(-L/2, L/2) \cap \mathbb{N}$ .

Let

$$\tilde{\nu} = \nu + i\mathcal{H}\nu \quad (27)$$

the analytic version of the background noise, and denote as  $\nu(k)$  and  $\nu_H(k)$  the (real-valued) samples, of the noise and its Hilbert transform.

For zero average Gaussian white noise with (two sided) power spectral density  $W_0$ , the spectral power density of analytic noise is

$$S_{\nu_a, \nu_a} = 4W_0 U[\theta(m)], \quad (28)$$

where  $U(\cdot)$  is Heaviside's function and  $\theta = 2\pi m/N \in (-\pi, \pi)$ ,  $N = 2L + 1$  being the number of DFT frequency samples.

It is a simple task to show that the first moment of the XWV is zero, in view of the assumed independence of the (Gaussian) noises in different detectors.

We now compute the second moment, viz.:

$$\begin{aligned} \sigma^2(n, m) &= E \{ W_{\nu_a, \mu_a}[n, \theta(m)] W_{\nu_a, \mu_a}^*[n, \theta(m)] \} = \\ &= \sum_{k=-L}^L \sum_{p=-L}^L E[\nu_a(n+k) \mu_a^*(n-k) \nu_a^*(n+p) \mu_a(n-p)] e^{-i2(k-p)\theta(m)} = \\ &= \sum_{k=-L}^L \sum_{p=-L}^L E[\nu_a(n+k) \nu_a^*(n+p)] E[\mu_a(n-p) \mu_a^*(n-k)] e^{-i2(k-p)\theta(m)} = \\ &= \sum_{k=-L}^L \sum_{p=-L}^L R_{\nu_a, \nu_a}^2(k-p) e^{-i2(k-p)\theta(m)} \end{aligned} \quad (29)$$

where  $\nu_a$  and  $\mu_a$  are built from independent, zero average, white(ned) Gaussian noises pertinent to different detectors, but assumed as having the same power spectral density  $W_0$ , and  $R_{\nu_a, \nu_a}(h-k) = E[\nu_a(h) \nu_a^*(k)]$  denotes the autocorrelation function of analytic noise. The inner summation in (29) can be extended to  $\infty$ , and the Wiener Khinchin theorem can be invoked to prove that,

$$\begin{aligned} \sigma^2(n, m) &\approx \sum_{k=-L}^L \sum_{p=-\infty}^{\infty} R_{\nu_a, \nu_a}^2(k-p) e^{-i2(k-p)\theta(m)} = \\ &= \sum_{k=-L}^L S_{\nu_a, \nu_a}[2\theta(m)] * S_{\nu_a, \nu_a}[2\theta(m)] = \end{aligned}$$

$$= 16W_0^2 \sum_{k=-L}^L \left| \frac{\theta}{\pi} \right| = (2L+1)16W_0^2 \left| \frac{\theta}{\pi} \right| = 32W_0^2 |m| \quad (30)$$

where  $m \in [-L/2, L/2] \cap \mathbb{N}$ .

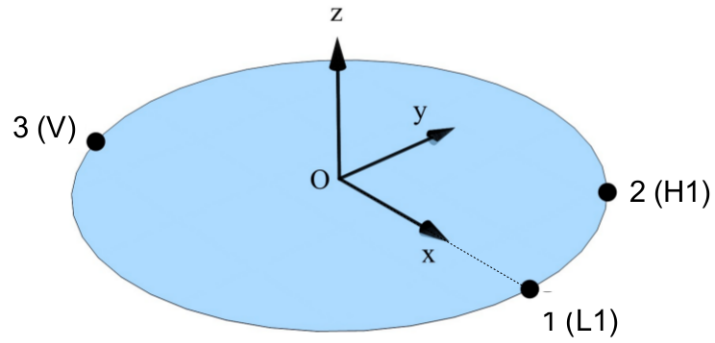


Figure 1 - Detectors' plane, and reference system.

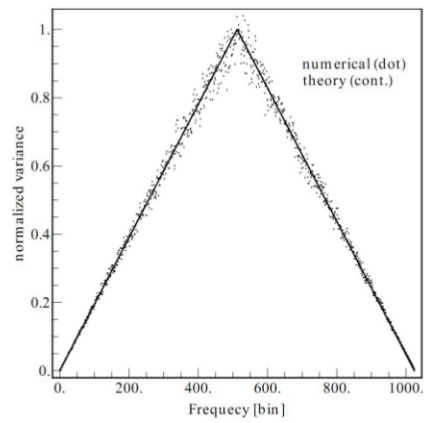


Figure 2 – Normalized variance of XWV of stationary Gaussian noise vs. frequency (fixed time-slice).



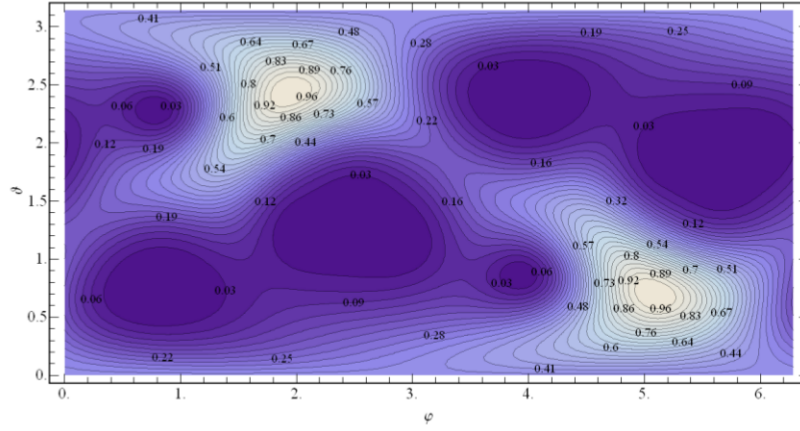


Figure 3 - Normalized directional response of proposed network detection statistic (H1-L1-V network, circular polarization).

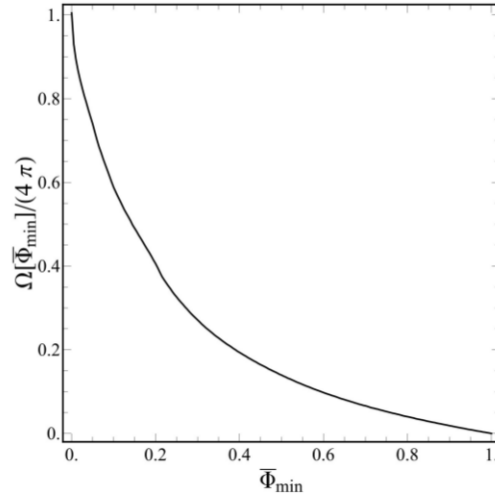


Figure 4 - Angular fraction of celestial sphere where normalized directional response exceeds a given level  $\bar{\Phi}_{min}$ .

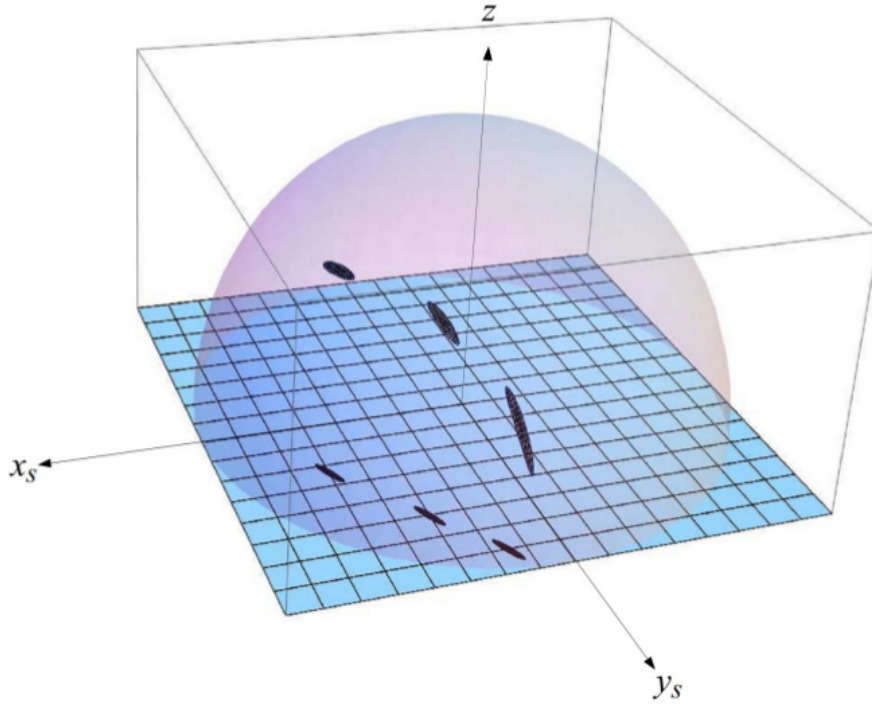


Figure 5 - Uncertainty areas on the celestial sphere and the detectors' plane for some source positions.

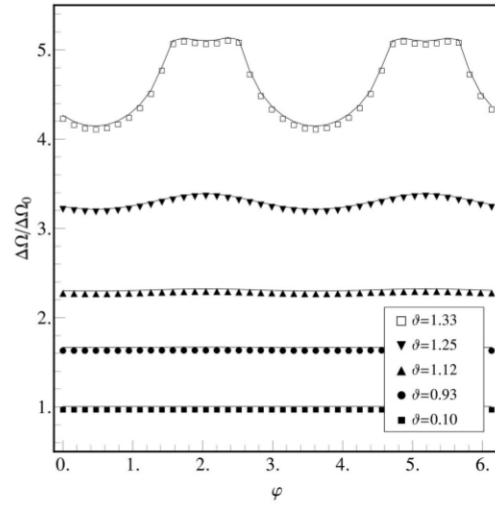


Figure 6a - Ratio between the uncertainty areas on the celestial sphere ( $\Delta\Omega$ ) and the detectors' plane ( $\Delta\Omega_0$ ) vs. source position ( $\vartheta, \varphi$ ).

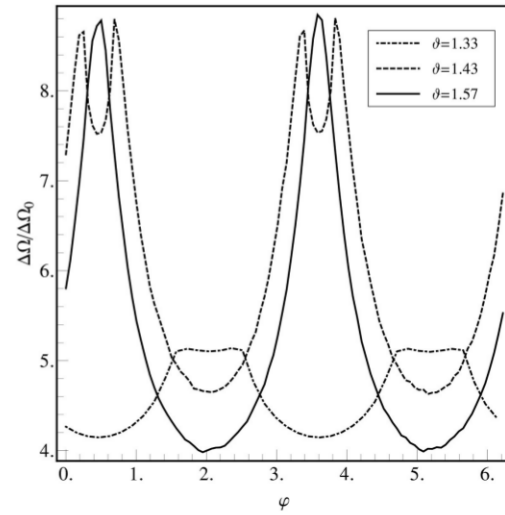


Figure 6b - Ratio between the uncertainty areas on the celestial sphere ( $\Delta\Omega$ ) and the detectors' plane ( $\Delta\Omega_0$ ) vs. source position ( $\vartheta, \varphi$ ).

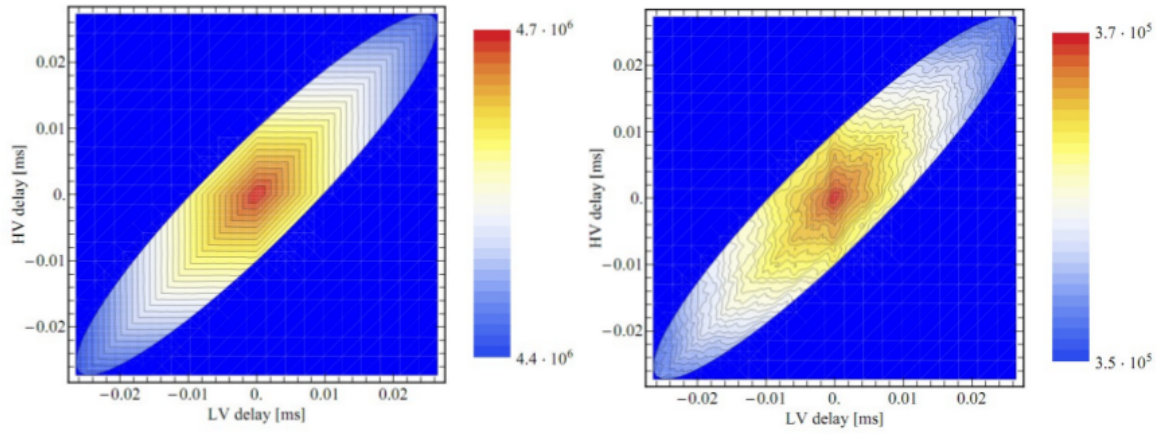


Figure 7 - Expected value (left) and standard deviation (right) of proposed network detection statistic. Gaussian noise only.

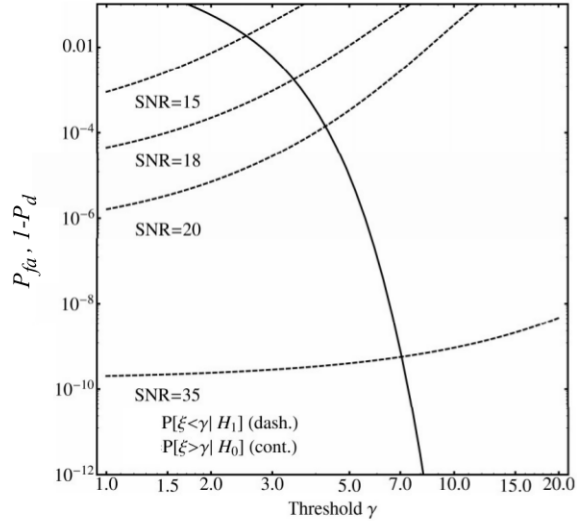


Figure 8a - False alarm and false dismissal probability vs. threshold, for various values of the intrinsic SNR ( $\delta_h$  in eq. 24). Source at maxima of the pattern function in Fig. 3.

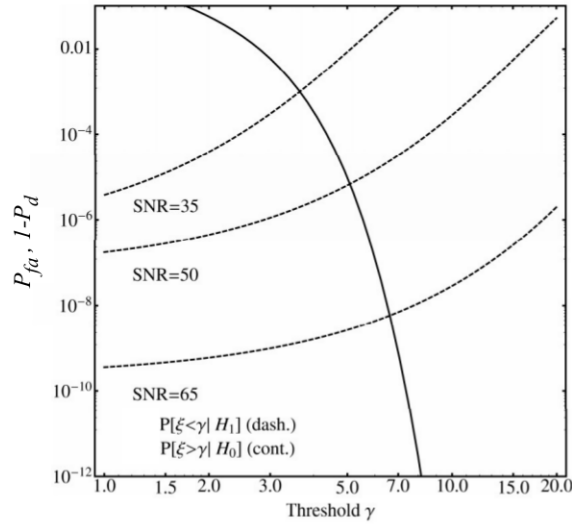


Figure 8b - False alarm and false dismissal probability vs. threshold, for various values of the intrinsic SNR ( $\delta_h$  in eq. 24). Source at minima of the pattern function in Fig. 3.

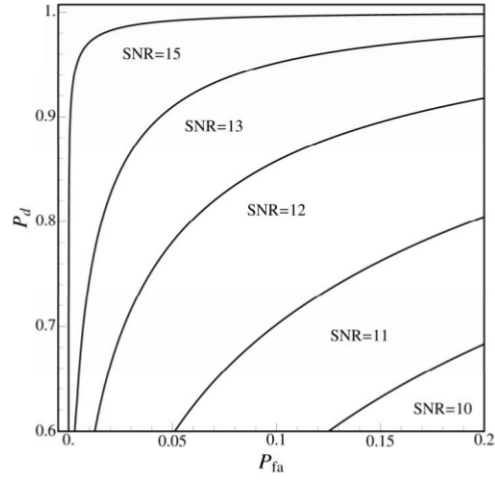


Figure 9a – ROCs, for various values of the intrinsic SNR ( $\delta_h$  in eq. 24).  
Source at maxima of the pattern function in Fig. 3.

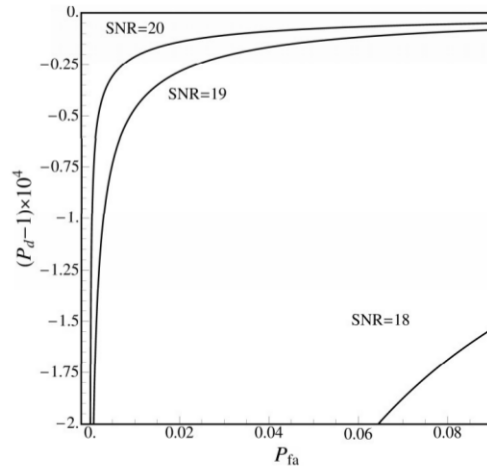


Figure 9b – ROCs, for various values of the intrinsic SNR ( $\delta_h$  in eq. 24).  
Source at maxima of the pattern function in Fig. 3.

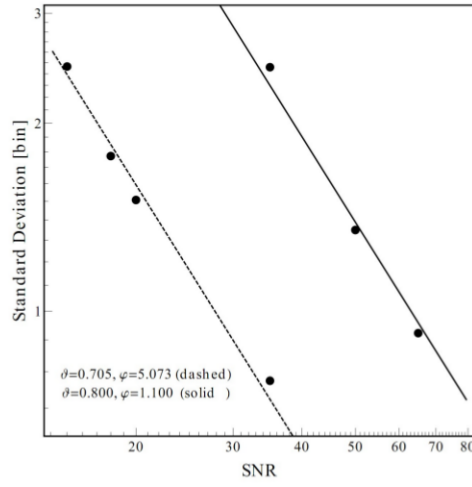


Figure 10 - Standard deviation (in time bins) of estimated arrival times vs. intrinsic SNR ( $\delta_h$  in eq. 24). Source at maxima (dashed line) and minima (solid line) of the pattern function in Fig. 3.

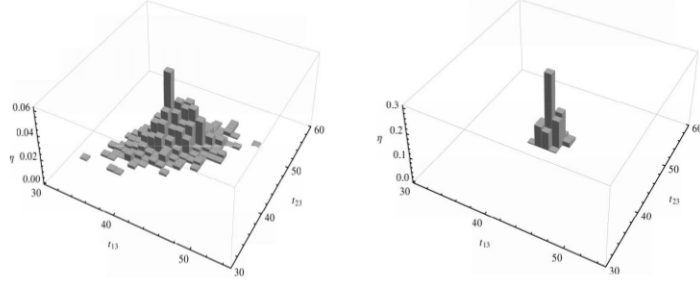


Figure 11a - Normalized binning (histogram) of estimated time delays, for two representative values of the intrinsic SNR:  $\delta_h=15$  (left) and  $\delta_h=35$  (right). Source at maximum of pattern function in Fig. 3.

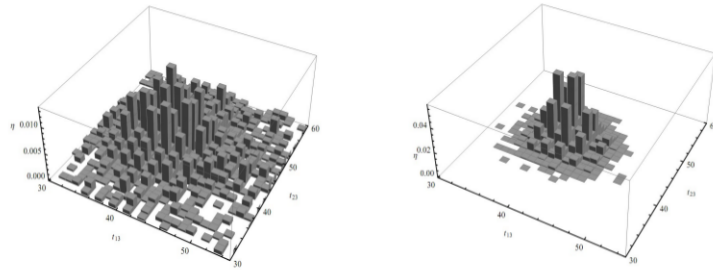


Figure 11b – Same as Fig. 11a, but a standard correlation-based time delay estimator has been used to retrieve the propagation delays  $t_{12}, t_{13}$ .



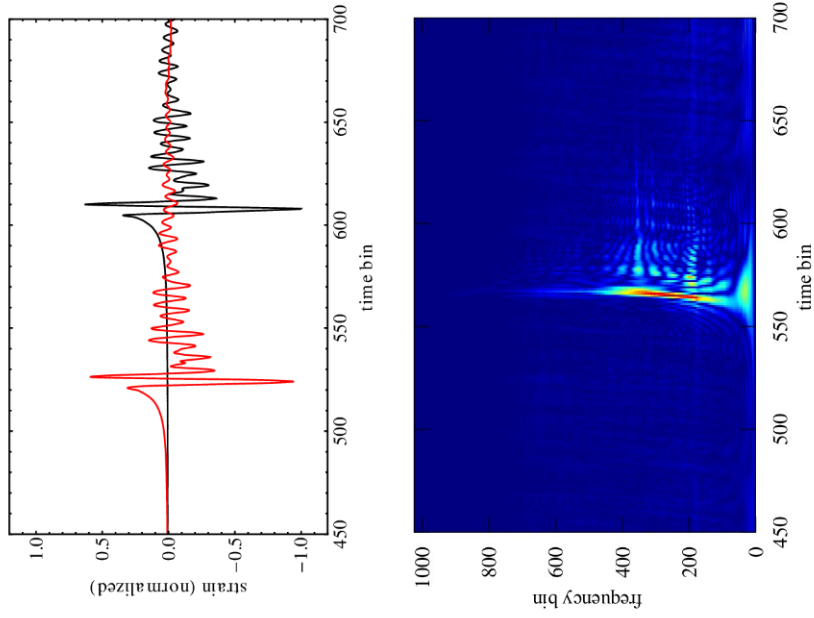


Figure 12 – Supernova core collapse GWBs according to Dimmelmaier (top), and XWV transform (bottom).

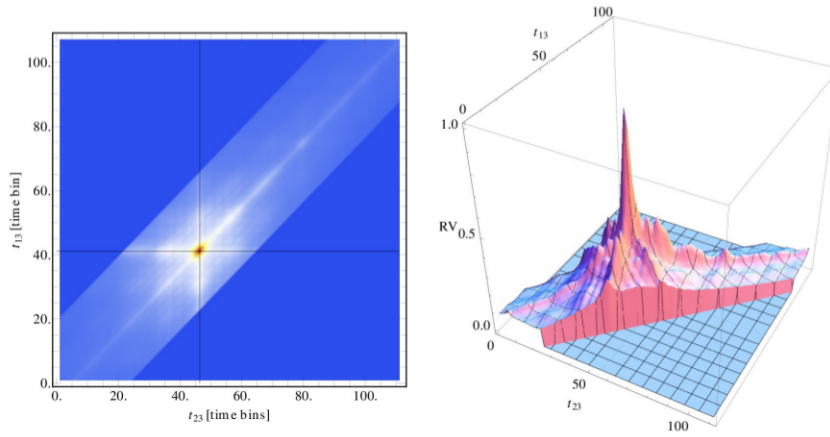


Figure 13 – Normalized density (left) and surface plot (right) of time-delay grid levels. Supernova core-collapse GWB (Dimmelmaier).  
Source at maximum of pattern function in Fig. 3.

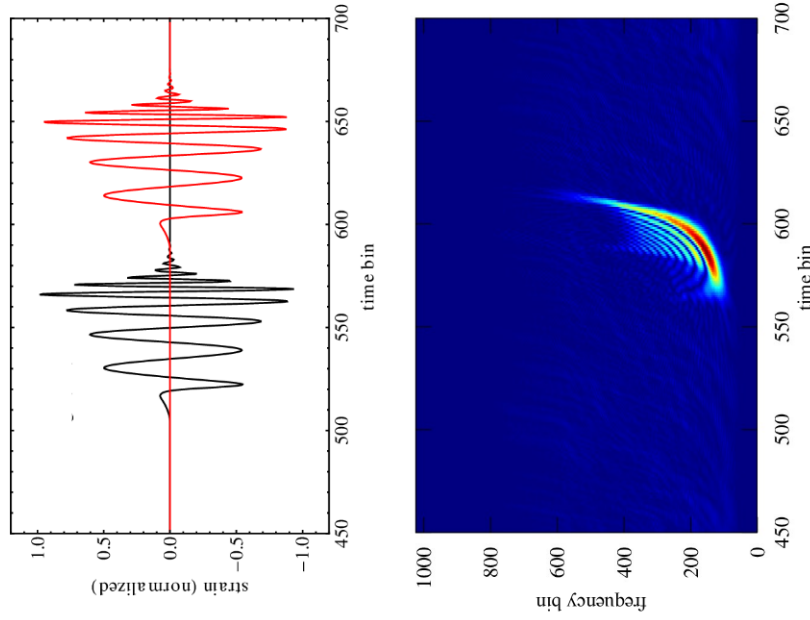


Figure 14 – Binary merger GWBs according to Baker (top), and XWV transform (bottom).

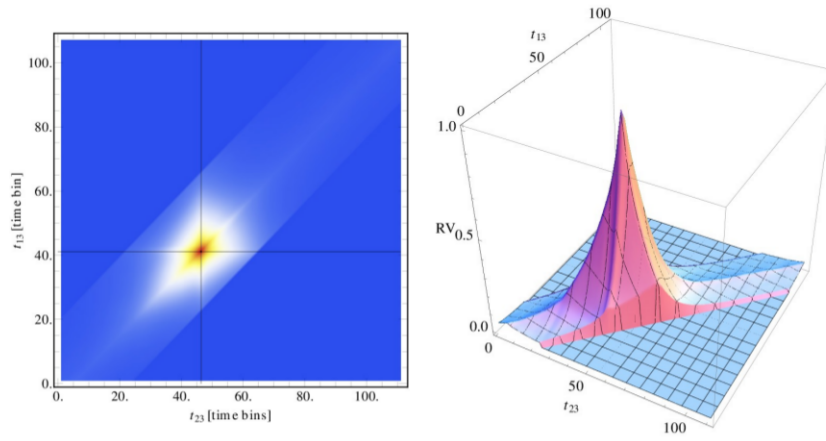


Figure 15 – Normalized density (left) and surface plot (right) of time-delay grid levels. Binary merger GWB (Baker).  
Source at maximum of pattern function in Fig. 3.

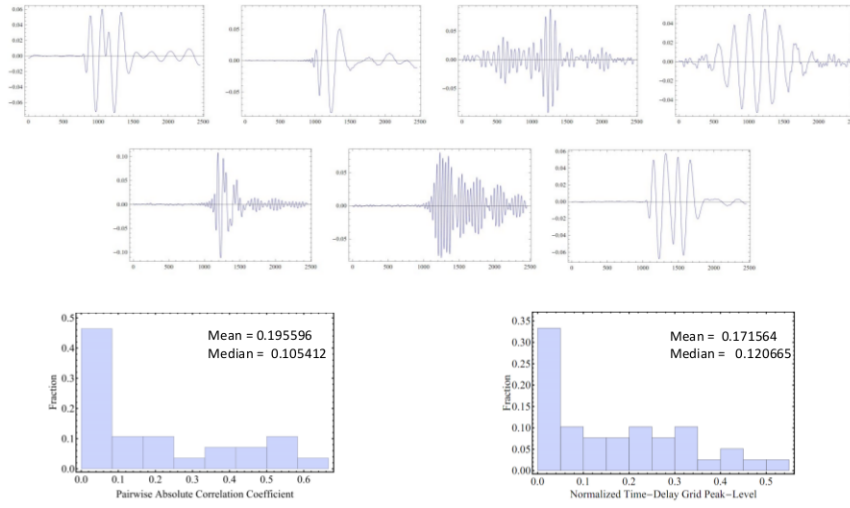


Figure 16 – Top: set of typical glitches (amplitude vs time bin) from [42], scaled to unit energy. Bottom left: histogram of related pairwise correlation coefficients. Bottom right: histogram of normalized time-delay grid-peak levels for triplets of different glitches.

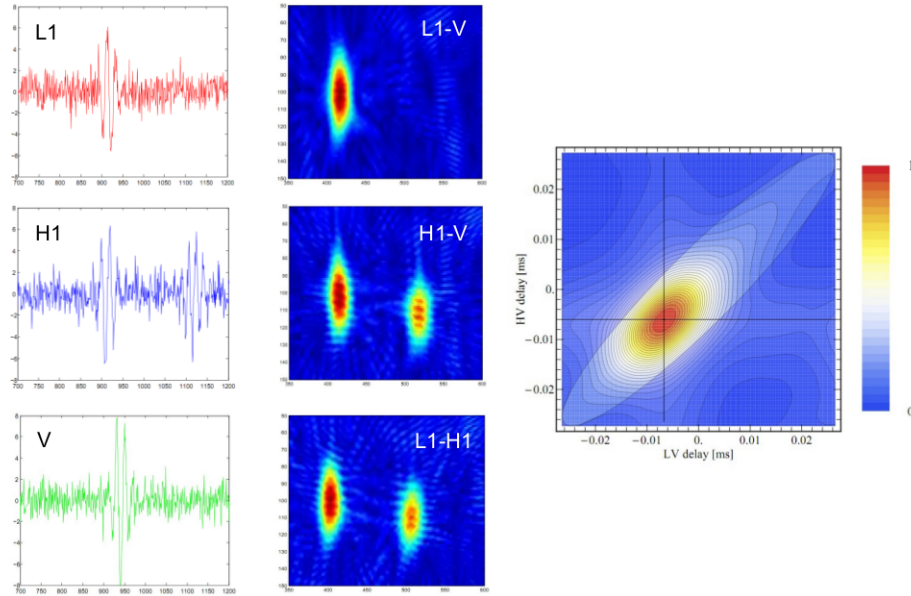


Figure 17 – GWB and single glitch (non overlapping) in one detector (H1). Left: waveforms; Mid: XWV spectra; Right: normalized density plot of time delay grid levels.

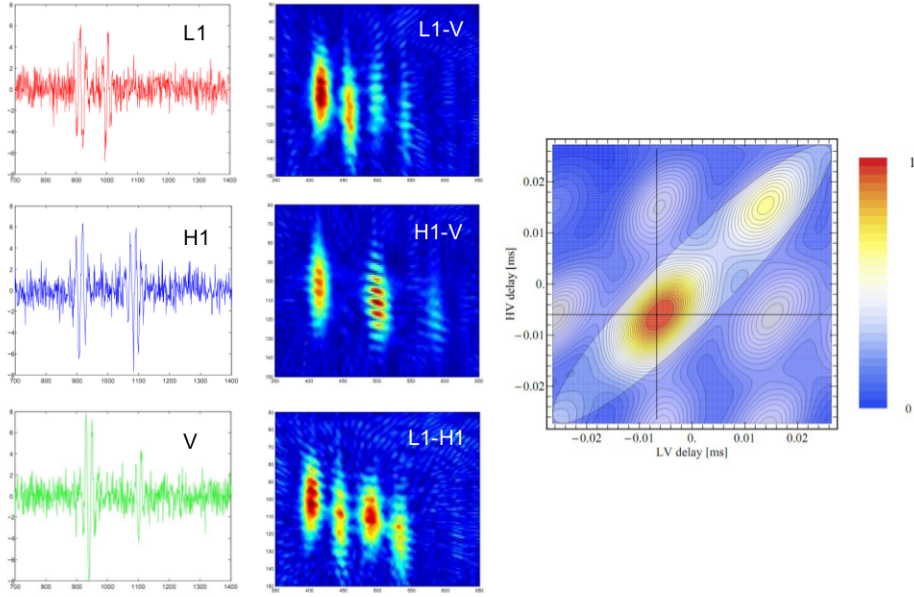


Figure 18 – GWB and single glitch (non overlapping) in each detector. Left: waveforms;  
Mid: XWV spectra; Right: normalized density plot of time delay grid levels.

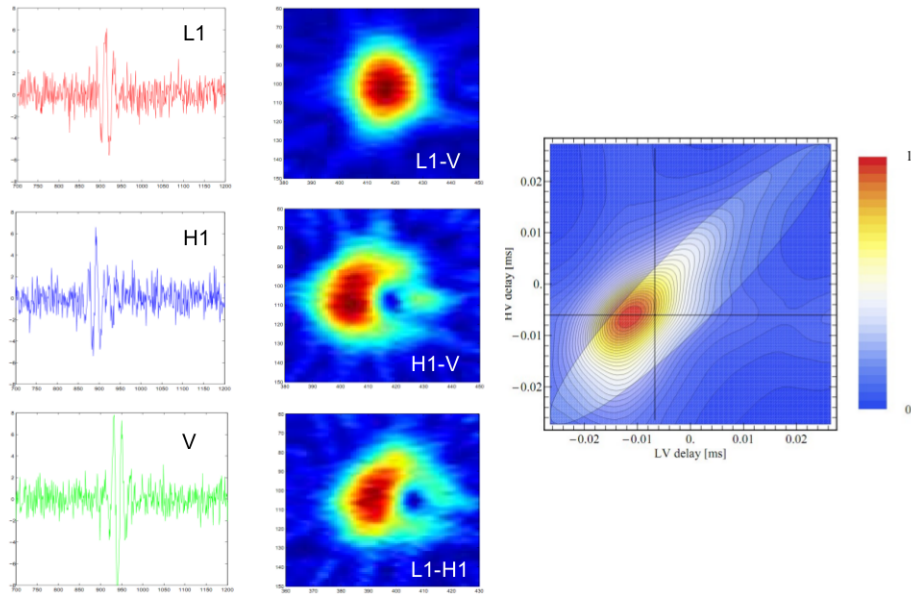


Figure 19 – GWB and single glitch (overlapping) in one detector (H1). Left: waveforms;  
Mid: XWV spectra; Right: normalized density plot of time delay grid levels.

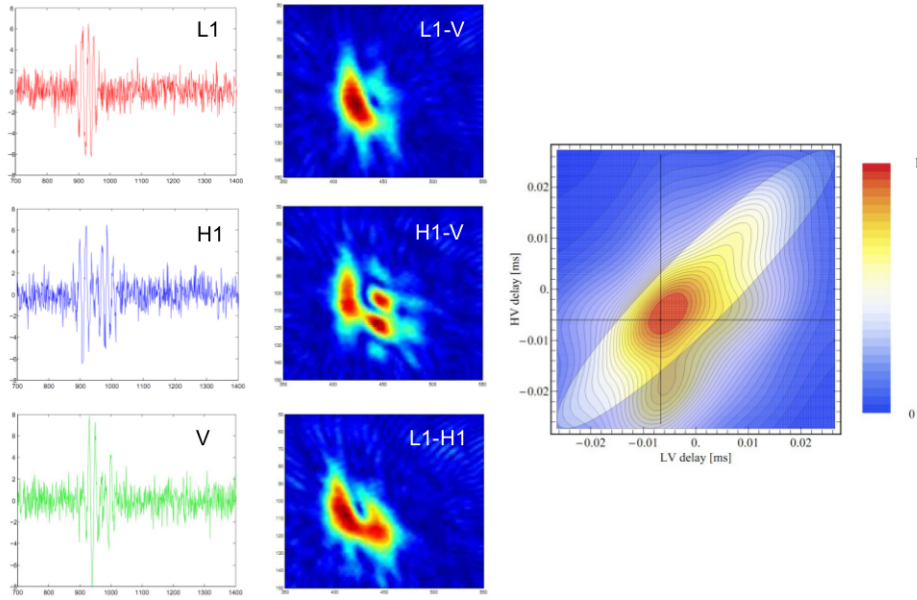


Figure 20 – GWB and single glitch (overlapping) in each detector. Left: waveforms; Mid: XWV spectra; Right: normalized density plot of time delay grid levels.